

# Stability of ternary interfaces and its effects on ideal switching characteristics in inverted coplanar organic transistors

Keito Murata<sup>1,\*</sup>, Gyo Kitahara<sup>1</sup>, Satoru Inoue<sup>1</sup>, Toshiki Higashino<sup>2</sup>, Satoshi Matsuoka<sup>1</sup>, Shunto Arai<sup>1,†</sup>, Reiji Kumai<sup>3</sup>, and Tatsuo Hasegawa<sup>1</sup>

<sup>1</sup>Department of Applied Physics, The University of Tokyo, Tokyo 113-8656, Japan

<sup>2</sup>National Institute of Advanced Industrial Science and Technology (AIST), Tsukuba 305-8565, Japan

<sup>3</sup>Photon Factory, Institute of Materials Structure Science, High Energy Accelerator Research Organization (KEK), Tsukuba 305-0801, Japan

(Received 3 May 2023; revised 18 July 2023; accepted 22 December 2023; published 2 February 2024)

Inverted coplanar or bottom-gate bottom-contact (BGBC)-type thin-film transistors (TFTs) present several advantages for the manufacture and application of organic TFTs, although serious difficulties are encountered when trying to achieve sufficiently high performance. Recently, it was demonstrated that both high mobility and ideal ON-OFF switching are attainable in BGBC-type printed organic TFTs with highly clean semiconductor-gate dielectric interfaces. However, an unknown channel material dependence in the device performance is found. Here, we show that the stability of semiconductor/metal/dielectric ternary interfaces is a crucial factor in the operation of BGBC-type organic TFTs. We fabricate single-crystal organic semiconductor (OSC) films with various numbers of layers using two different materials (phenyl/alkyl-substituted benzothieno[3,2-*b*]benzothiophene and phenyl/alkyl-substituted benzothieno[3,2-*b*]naphtho[2,3-*b*]thiophene) on highly lyophobic Cytop gate dielectric surfaces. The transfer characteristics exhibit notable time-dependent degradation, which clearly depends on the material, layer number, and encapsulation. Kelvin-probe force microscopy measurements reveal that the degradation is ascribed to contact resistance at the source electrodes, while it can be more suppressed in multilayer (two or more layers) OSCs. Atomic force microscopy and in-plane x-ray diffraction profiles present signs of the transformation in single molecular bilayer OSCs laid on the electrodes. The results suggest the importance of the quality of the OSC layer at ternary interfaces, providing a clue for improving the performance of BGBC-type organic TFTs.

DOI: 10.1103/PhysRevApplied.21.024005

## I. INTRODUCTION

For wide application of organic thin-film transistors (TFTs), improvements are required in the performance indexes of electrical characteristics, such as device mobility, switching sharpness, operation voltage, and operation stability. It is expected that the parasitic resistance of the semiconductor bulk arising between the channel and the source or drain electrodes can be reduced by adopting coplanar [bottom-gate bottom-contact (BGBC) or top-gate top-contact] TFTs, which are in principle more

advantageous than staggered [bottom-gate top-contact (BGTC) or top-gate bottom-contact] TFTs. This is simply because vertical transport across the channel layer is necessary in the latter [1]. Additionally, inverted coplanar or BGBC-type TFTs are more promising for practical uses, because this type of device should allow a variety of manufacturing processes to be used for the stacking and patterning of electrode and/or dielectric components without having adverse effects on the organic semiconductor (OSC) channel layer [2–4].

Meanwhile, it is known to be quite difficult to obtain BGBC-type organic TFTs that exhibit sufficiently high performance, as compared to BGTC-type organic TFTs that are utilized as standard. It has been pointed out for vacuum-deposited polycrystalline BGBC-type organic TFTs that the crystal growth mode of the OSC layer on an electrode surface or edge is distinct from that on a gate dielectric surface, which eventually limits the carrier injection and device performance [2,5–8]. Furthermore, there are often serious unknown difficulties when

\*murata@hsgw.t.u-tokyo.ac.jp

<sup>†</sup>Present address: National Institute for Materials Science (NIMS), Tsukuba, Ibaraki 305-0044, Japan.

Published by the American Physical Society under the terms of the [Creative Commons Attribution 4.0 International license](#). Further distribution of this work must maintain attribution to the author(s) and the published article's title, journal citation, and DOI.

trying to achieve high performance in BGBC-type organic TFTs composed of either polycrystalline or single-crystal OSC films fabricated either by solution or vacuum processing [9–11]. One problem is that the origin of the performance deterioration is not understood, although a few recent studies have reported high device performance in BGBC-type organic TFTs [3,12–14]. The following aspects have been proposed as the origin of the deterioration: (1) the applied electric field from the gate does not work effectively for carrier injection [15–17]; (2) space charge accumulates at the conduction path [18–20]; and (3) other effects [4,7,21–26]. Thus far, a way of constructing ideal BGBC-type organic TFTs has not been clarified or established.

Recently, it was reported that both high mobility and ideal ON-OFF switching are attainable in solution-processed BGBC-type organic TFTs [10]. A notable feature is that the devices exhibit extremely sharp switching characteristics close to the theoretical limit, which is ascribed to the formation of highly clean semiconductor-gate dielectric interfaces with the use of the highly lyophobic Cytop. The production of such interfaces was enabled by adopting the extended meniscus-guided (EMG) coating technique. However, it was also shown that the device mobility strongly depends on the OSC channel material. The mobility value is more than 10 times lower than that of BGTC-type TFTs for phenyl/alkyl-substituted benzothieno[3,2-*b*]benzothiophene (Ph-BTBT-C<sub>*n*</sub>) [27–29], while a

comparably high value is obtained for phenyl/alkyl-substituted benzothieno[3,2-*b*]naphtho[2,3-*b*]thiophene (Ph-BTNT-C<sub>*n*</sub>) [30–32]. [The molecular structures of Ph-BTBT-C<sub>*n*</sub> and Ph-BTNT-C<sub>*n*</sub> are shown in Fig. 1(a)]. We consider that the observed channel material dependence is associated with the unknown problem at the semiconductor-metal-dielectric ternary interfaces, and thus offers a unique opportunity to clarify why many BGBC-type TFTs fail to operate.

In this study, we investigate the operations of sharp-switching BGBC-type organic TFTs based on both Ph-BTBT-C<sub>*n*</sub> and Ph-BTNT-C<sub>*n*</sub>. We focus on the dependence of the device characteristics on the number of layers of single-crystal OSC films and on their temporal variations. We find that the devices composed of single molecular bilayer films of Ph-BTBT-C<sub>*n*</sub> exhibit rapid and notable degradation of the device characteristics, while the degradation is evidently suppressed by using multilayer (two or more layers) films, Ph-BTNT-C<sub>*n*</sub> films, or by encapsulation. We use Kelvin-probe force microscopy (KPFM) to investigate the electric potential variation along the channel, and we also investigate the OSC film morphology around the ternary interfaces using atomic force microscopy (AFM) and x-ray diffraction (XRD) measurements. Based on the results, we discuss the origin of the degradation in the device characteristics, and the important roles of the ternary interfaces in BGBC-type organic TFTs.

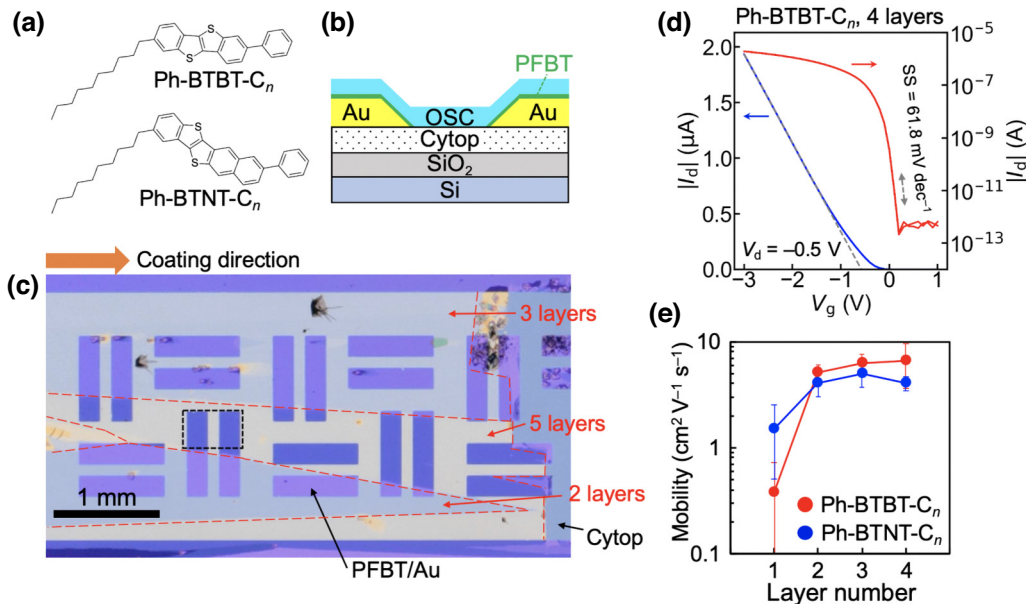


FIG. 1. Single-crystal TFTs with various numbers of layers of OSC films. (a) Chemical structures of Ph-BTBT-C<sub>*n*</sub> and Ph-BTNT-C<sub>*n*</sub>. (b) Schematic cross section of TFTs. (c) Optical image of various numbers of layers of OSC films with a mixed solution of Ph-BTBT-C<sub>*n*</sub>. The red dashed line shows the boundary between regions with uniform thickness of OSC films. The black dashed line rectangle shows one of the TFTs with a uniform layer number. (d) Transfer characteristics of four layers of Ph-BTBT-C<sub>*n*</sub> TFTs. The mobility value is estimated as  $9.1 \text{ cm}^2 \text{ V}^{-1} \text{ s}^{-1}$ . The SS value is extracted by the linear fit of current slope in the range from  $|I_d| = 10^{-11.5}$  to  $10^{-10} \text{ A}$ . (e) Layer-number dependence of the device mobility in the linear regime several days after device fabrication.

## II. EXPERIMENT

### A. Manufacturing BGBC-type TFTs with different numbers of layers

Figure 1(b) schematically shows a cross section of the BGBC-type organic TFTs that we produce. We use heavily *p*-doped silicon plates with a 100-nm-thick surface SiO<sub>2</sub> layer as substrates. The Cytop layer is spin-coated (at 2000 rpm for 60 s) using a solution of Cytop (CTL-809M; AGC Inc., Japan) diluted with the solvent (CT-Solv.180; AGC Inc., Japan) at a ratio of 1:4. The Cytop layer is then cured in a vacuum oven (at 50 °C for 10 min at 0.08 MPa, 80 °C for 15 min at 0.02 MPa, and 180 °C for 60 min at 0.02 MPa). To form the source and drain electrodes and U-shaped metal guide required for the EMG coating (see Supplemental Material Fig. S1 [33]), 0.5-nm-thick Cr and 25-nm-thick Au are vacuum deposited through a shadow mask on top of the Cytop layer. The electrode surface is modified by chemical vapor treatment with pentafluorobenzenethiol (PFBT) (>95.0%; Tokyo Chemical Industry Co., Ltd., Japan).

The OSC materials are synthesized according to the literature [30,34]. It is reported that the use of a mixed solution of OSCs with different alkyl chain lengths effectively suppresses the multiple stacking of molecular bilayer films [10,35]. Thus, we use a mixture of Ph-BTBT-C<sub>10</sub> and Ph-BTBT-C<sub>14</sub> for fabricating Ph-BTBT-C<sub>n</sub> films, and a mixture of Ph-BTNT-C<sub>10</sub> and Ph-BTNT-C<sub>12</sub> for fabricating Ph-BTNT-C<sub>n</sub> films. The respective compounds are dissolved in chlorobenzene (Wako Special Grade; Fujifilm Wako Pure Chemical Corp., Japan) at 0.05 or 0.1 wt %. The solutions are mixed at different mixing ratios to control the layer-number thickness of single-crystal OSC films by the moderate suppression of the multiple stacking of bilayer units. For example, we utilize a volume ratio of 9:1 (Ph-BTBT-C<sub>10</sub>:Ph-BTBT-C<sub>14</sub>) to fabricate single molecular bilayer films (hereafter referred to as single-layer films), and a ratio of 97:3 to obtain films with several layers (hereafter referred to as multilayer films), as presented in Fig. S1 in the Supplemental Material [33]. Finally, the EMG coating technique is used to obtain uniform larger-area single-crystal OSC films on the Cytop surface under ambient pressure and temperature. The fabricated films are dried under ambient temperature.

The TFT channel is isolated from unnecessary parts by removing the outside OSC films with uniform thickness using a micromanipulator (Axis Pro; Micro Support Co., Ltd., Japan), as shown in Fig. S2 in the Supplemental Material [33]. Optical microscope images and crossed-Nicols micrographs are collected with a digital microscope (VHX-6000; Keyence Corp., Japan). The layer number of the channel semiconductor layer is determined using AFM (VN-8010; Keyence Corp., Japan).

### B. Device and thin-film characterization

The electrical characteristics are measured in a glove box filled with N<sub>2</sub> gas using a semiconductor parameter analyzer (E5270A; Agilent Technologies Inc., USA). The channel length *L* is 100 μm. The channel width *W* varies from device to device, ranging from 100 to 800 μm, as the areas with uniform thickness are selected from the single-crystal OSC films [see Figs. 1(c) and S2 in the Supplemental Material [33]]. The gate capacitance is estimated as 22 nF cm<sup>-2</sup>, composed of the series capacitance of Cytop and SiO<sub>2</sub>, with relative permittivity 2.0 and 3.9 and thickness 30 and 100 nm. To encapsulate the OSC channel layer of the TFTs, we use another Cytop layer that is spin-coated with a solution diluted with solvent to a ratio of 1:1 with solvent on top of the devices and heated at a temperature below the glass transition point (108 °C). The thickness of the encapsulating film is about 200 nm.

KPFM measurements and observation of the surface morphology of the OSC films are conducted with MFP-3D (Asylum Research, USA). The in-plane XRD measurements are conducted by a thin-film diffractometer (SOR-SmartLab; Rigaku Co., Ltd., Japan) installed in the beamline BL-7C at the Photon Factory, High-Energy Accelerator Research Organization (KEK). Diffraction intensity is recorded using a scintillation counter.

## III. RESULTS AND DISCUSSION

### A. Material and layer-number dependence of device mobility

We successfully obtain OSC films with various layer numbers on top of the Cytop layer and source and drain electrodes for both Ph-BTBT-C<sub>n</sub> and Ph-BTNT-C<sub>n</sub>, as presented in Figs. 1(c) and S2 in the Supplemental Material [33]. The OSC films are stacked only in bilayer units within very large single-domain crystal films, as confirmed by AFM measurements and crossed-Nicols polarized microscope observation. The BGBC-type TFTs with different layer-number thicknesses are fabricated by extracting the OSC films with uniform thickness areas, as shown in Fig. 1(c). We find that almost all devices exhibit turn-on voltage (*V*<sub>on</sub>) around 0 V, sharp switching with the subthreshold swing (SS) value of 60–80 mV dec<sup>-1</sup>, and negligible hysteresis, regardless of the thickness or the OSC material, as shown in Fig. 1(d). We observe clear dependence of the ON current on the thickness of the OSC films, associated with the difference in the device mobility.

Figure 1(e) summarizes layer-number dependence of the device mobility for both Ph-BTBT-C<sub>n</sub> and Ph-BTNT-C<sub>n</sub> TFTs, measured a few days after device fabrication. The single-layer TFTs of Ph-BTNT-C<sub>n</sub> exhibit higher mobility than those of Ph-BTBT-C<sub>n</sub>, as consistent with a previous report [10]. Importantly, multilayer TFTs exhibit much higher mobility than single-layer TFTs based on

the same OSCs. Note that the difference owing to the layer-number dependence is much larger than the difference expected from the in-plane anisotropy of the crystal films [35]. It is worth mentioning that the multilayer TFTs of Ph-BTBT-C<sub>n</sub> exhibit a higher mobility (average value of  $6 \text{ cm}^2 \text{ V}^{-1} \text{ s}^{-1}$ ) than those of Ph-BTNT-C<sub>n</sub> (average value of  $4 \text{ cm}^2 \text{ V}^{-1} \text{ s}^{-1}$ ), for which the material dependence is reversed compared with the case of single-layer TFTs. Nonetheless, the material dependence of the multilayer TFTs is rather similar to that of the BGTC-type single-crystal TFTs [27–31].

## B. Time-dependent TFT characteristics and effects of encapsulation

Figures 2(a) and S3 in the Supplemental Material [33] show the temporal variation in the transfer characteristics of the respective TFTs with different layer numbers or OSC materials, measured repeatedly after device fabrication. No voltage is applied between the measurements. The characteristics exhibit a strong time dependence, and depend on the layer number and materials, as seen in Fig. 2(b). Single-layer TFTs composed of Ph-BTBT-C<sub>n</sub> exhibit

mobility at  $4 \text{ cm}^2 \text{ V}^{-1} \text{ s}^{-1}$  immediately after device fabrication, whereas a gradual but significant degradation of the ON current is observed within 200 h. In contrast, the mobility of multilayer (three layers) TFTs is much more stable, with the initial high mobility of  $8 \text{ cm}^2 \text{ V}^{-1} \text{ s}^{-1}$  being maintained for up to 200 h. The distribution of mobility values is estimated at  $2\text{--}9 \text{ cm}^2 \text{ V}^{-1} \text{ s}^{-1}$  for both the single-layer TFTs measured immediately after device fabrication and the multilayer TFTs (see also Fig. S4 in the Supplemental Material [33]). Previous studies have reported a mobility of over  $10 \text{ cm}^2 \text{ V}^{-1} \text{ s}^{-1}$  for Ph-BTBT-C<sub>10</sub> [12,27–29], which is somewhat larger but close to the value observed in this study.

For Ph-BTNT-C<sub>n</sub>, the speed of degradation of the device mobility in single-layer TFTs varies greatly from device to device, as shown in Fig. S5 in the Supplemental Material [33]. The degradation of some devices proceeds much more slowly than for Ph-BTBT-C<sub>n</sub>. The results demonstrate that the observed layer-number and material dependence is associated with the difference in the speed of degradation. In contrast to the time-dependent degradation of mobility, we find that the turn-on voltage, switching sharpness, and hysteresis exhibit a high temporal stability; low-voltage operation below 3 V with a small SS

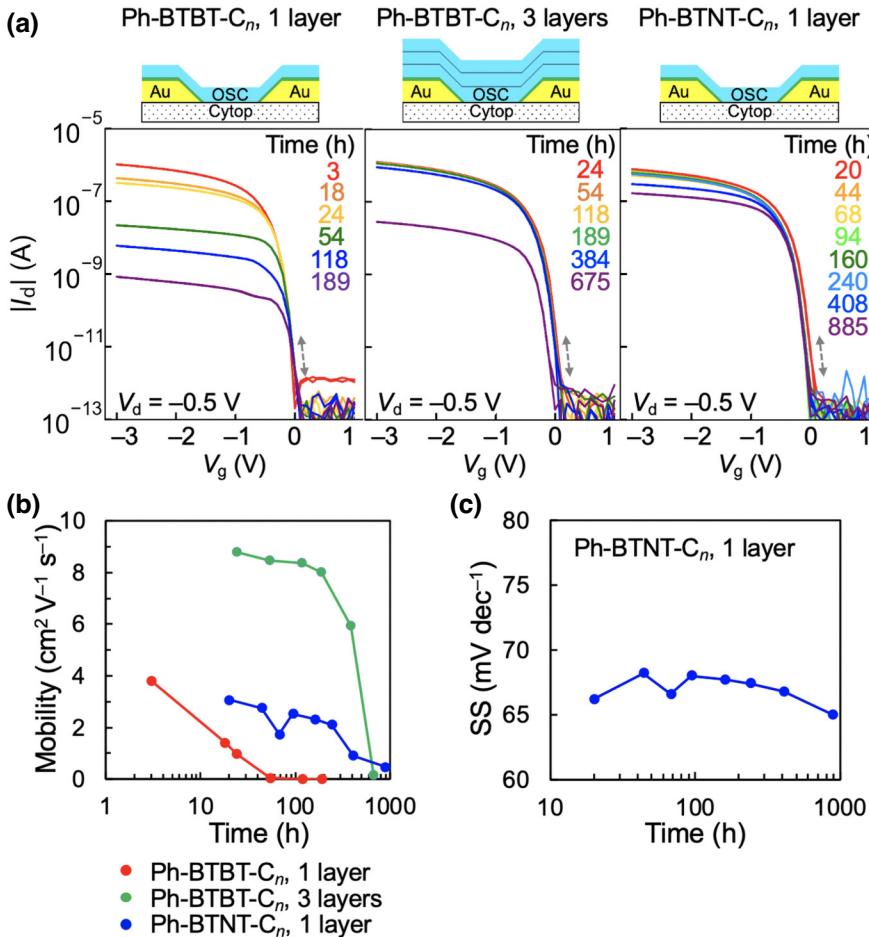


FIG. 2. Transfer characteristics of TFTs with various OSC materials and layer numbers. All devices are stored under nitrogen atmosphere. (a) Transfer curves in the linear regime measured at various times after device fabrication. The schematic of each device structure above the gate dielectric layer is also shown. (b) Temporal variation in the device mobility extracted from the transfer curves. (c) Temporal variation in the SS value of the single-layer Ph-BTNT-C<sub>n</sub> TFTs.

value of less than  $70 \text{ mV dec}^{-1}$  [Fig. 2(c)] is achieved. Even in the case of single-layer Ph-BTBT-C<sub>n</sub>, the SS value for most of the devices remains less than  $70 \text{ mV dec}^{-1}$  for up to 150 h. The results lead us to conclude that the varied time-dependent degradation of mobility in BGBC-type TFTs causes the apparent difference of the device mobility shown in Fig. 1(e), whereas the subthreshold characteristics are kept stable.

We also investigate the atmospheric effects on the temporal variation in the TFT characteristics. The single-layer Ph-BTBT-C<sub>n</sub> TFTs are subjected to various atmospheres (air, N<sub>2</sub> gas, and vacuum), and the temporal variation in the device characteristics are measured. We also measure the temporal variation for TFTs encapsulated by Cytop layers [Fig. 3(a)]. We did not observe any damage on the semiconductor layer due to the encapsulation process [see Fig. S6(a) in the Supplemental Material [33]]. We find that the degradation occurs at any atmospheric conditions up to 200 h, but not in the case of the encapsulated TFTs, as shown in Figs. 3(b) and S6 in the Supplemental Material [33]. The encapsulated TFTs exhibit exceptionally high stability while maintaining the initial mobility. Furthermore, we also observe an interesting feature in that the degradation of mobility is gradually saturated in air after 100 h, whereas this characteristic is further degraded in nitrogen gas for both Ph-BTBT-C<sub>n</sub> and Ph-BTNT-C<sub>n</sub>, as seen in Figs. 3(c) and S7 in the Supplemental Material [33]. In addition, drain or gate bias stress between each measurement does not affect degradation speed in the device characteristics (see Fig. S8 in the Supplemental Material [33]). Note that these results contrast with the general understanding that the degradation of TFT characteristics is attributed to the effects of exposure to ambient air and bias stress [36,37].

### C. Potential drop at ternary interfaces in BGBC-type TFTs

To investigate the origin of the degradation in device characteristics, we measure the local surface electric potential distribution along the channels using KPFM, which allows us to discriminate and compare the channel and contact resistance [38–40]. First, we use single-layer Ph-BTBT-C<sub>n</sub> TFTs and single-layer Ph-BTNT-C<sub>n</sub> TFTs in the KPFM measurements. Figure 4 shows the potential profiles through the channel area in the linear regime ( $V_d = -0.5 \text{ V}$ ,  $V_g = -3 \text{ V}$ ). In the respective measurements, we confirm that the drain potential is  $0.5 \text{ V}$  ( $=|V_d|$ ) lower than the source potential, while the potential profiles are changed considerably by the change in the gate voltage  $V_g$ , as seen in Fig. S9 in the Supplemental Material [33]. We observe that the electric potential decreases gradually along the channel in both the single-layer Ph-BTBT-C<sub>n</sub> TFTs and Ph-BTNT-C<sub>n</sub> TFTs immediately after device fabrication, as seen in Fig. 4(a). After 78 h, a potential

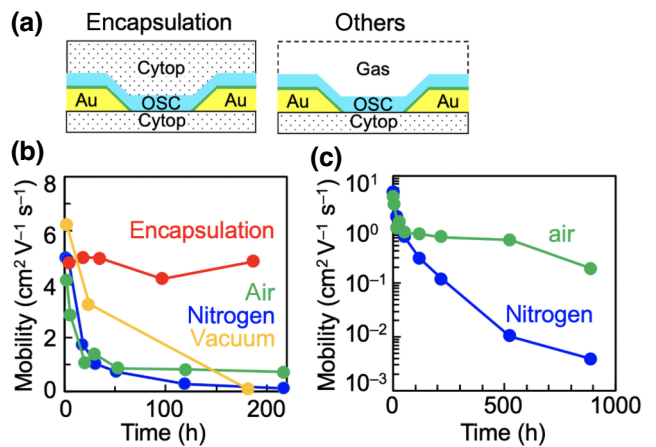


FIG. 3. Transfer characteristics of single-layer Ph-BTBT-C<sub>n</sub> TFTs under various atmospheres. (a) Device structures above the gate dielectric layer. (b),(c) Temporal variation in the device mobility. TFTs stored in a laboratory, in a glove box filled with N<sub>2</sub> gas, and in a chamber ( $10^{-4} \text{ Pa}$ ) are shown as “Air”, “Nitrogen,” and “Vacuum”, respectively.

drop around the boundary of the source electrode and channel increase significantly and the potential in the channel become almost flat in the single-layer Ph-BTBT-C<sub>n</sub> TFT. The single-layer Ph-BTNT-C<sub>n</sub> TFT also exhibits a similar potential drop at the source electrode edge after 79 h, although the drop is clearly smaller than that of the single-layer Ph-BTBT-C<sub>n</sub> TFT. The results indicate that the effective drain bias applied to the channel decreases with time in the single-layer TFTs, which proceeds more rapidly in Ph-BTBT-C<sub>n</sub> TFTs than in Ph-BTNT-C<sub>n</sub> TFTs.

To investigate the layer-number dependence of the potential distribution, we conduct KPFM measurements of the single-layer and multilayer (four layers) Ph-BTBT-C<sub>n</sub> TFTs that exhibit mobility of  $0.02 \text{ cm}^2 \text{ V}^{-1} \text{ s}^{-1}$  and  $6.0 \text{ cm}^2 \text{ V}^{-1} \text{ s}^{-1}$ , respectively. Figure 4(b) shows the potential profiles for single-layer and multilayer TFTs based on Ph-BTBT-C<sub>n</sub> and Ph-BTNT-C<sub>n</sub>. We observe a large and a small potential drop around the edges of the source and the drain electrodes, respectively, in the case of the single-layer Ph-BTBT-C<sub>n</sub> TFT. In contrast, the potential drop is negligibly small in the case of the multilayer Ph-BTBT-C<sub>n</sub> TFT, where the drain potential uniformly and gradually decreases along the channel. As seen on the two-dimensional maps of the surface potential shown in Fig. S10 in the Supplemental Material [33], these potential drops around the contacts are uniformly observed in the single-layer TFTs but not in multilayer TFTs. A similar trend is also observed in the saturation regime ( $V_d = -3 \text{ V}$ ,  $V_g = -3 \text{ V}$ ) (see Fig. S9 in the Supplemental Material [33]).

The potential drop observed at the electrode edge in the single-layer Ph-BTNT-C<sub>n</sub> TFTs is not considerable, but is slightly larger than that in the multilayer (two layers)

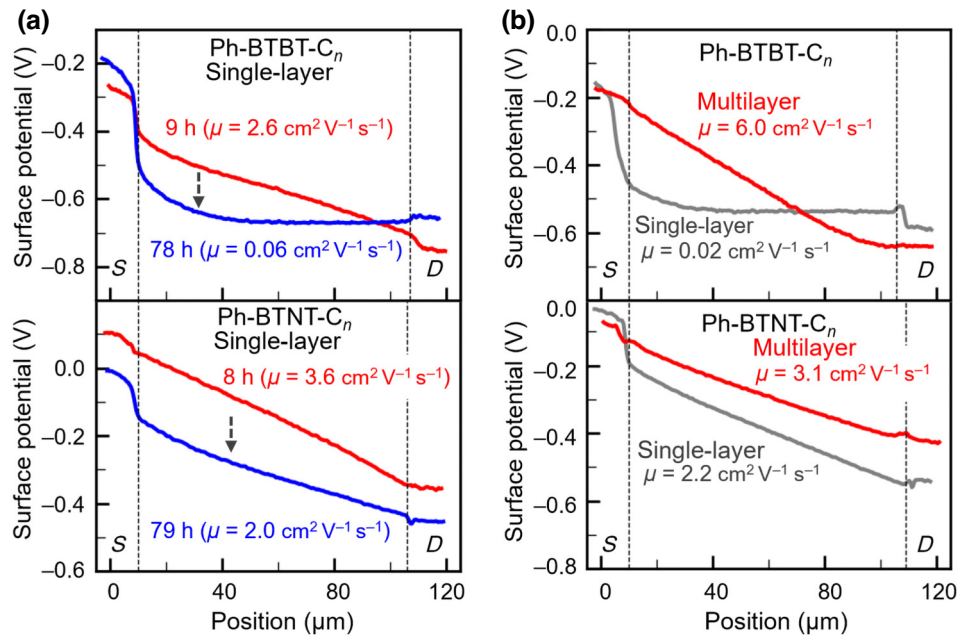


FIG. 4. Surface potential distribution in the linear regime ( $V_d = -0.5 \text{ V}$ ,  $V_g = -3 \text{ V}$ ) along the TFT channel. (a) Time dependence of surface potential of specific (upper) single-layer Ph-BTBT-C<sub>n</sub> and (lower) single-layer Ph-BTNT-C<sub>n</sub> TFTs. (b) Layer-number dependence of surface potential of (upper) Ph-BTBT-C<sub>n</sub> and (lower) Ph-BTNT-C<sub>n</sub> TFTs, respectively. Ph-BTBT-C<sub>n</sub> and single-layer Ph-BTNT-C<sub>n</sub> TFTs are measured within 20–40 h. The multilayer Ph-BTNT-C<sub>n</sub> TFTs are measured at approximately 250 h. “S” and “D” correspond to source and drain electrodes, respectively. Each dashed line represents the boundary between the electrode and the channel.

TFTs. The layer-number dependence is basically similar between Ph-BTBT-C<sub>n</sub> and Ph-BTNT-C<sub>n</sub>, whereas the potential drop in Ph-BTNT-C<sub>n</sub> is much smaller than that in Ph-BTBT-C<sub>n</sub>. These features are consistent with the trend of the device mobility; the TFTs with higher mobility exhibit a smaller potential drop. Thus, we conclude that the degradation of the device mobility depending on layer number and material is attributed to the contact resistance. This means that the contact resistance should increase with time, especially in single-layer Ph-BTBT-C<sub>n</sub> and Ph-BTNT-C<sub>n</sub> TFTs.

To evaluate the sheet resistance of the OSC channels separately from the contact resistance, we also apply the transfer line method (TLM) for the single-layer and multilayer Ph-BTBT-C<sub>n</sub> TFTs. The results are shown in Fig. S11 in the Supplemental Material [33]. From the results, we find that the slope in the TLM plot (corresponding to the sheet resistance) remains constant with time, whereas the intercept at  $L = 0 \text{ }\mu\text{m}$  (corresponding to the contact resistance) increases gradually with time. We evaluate the sheet resistance as 3.0–3.3  $\text{M}\Omega/\text{sq}$  for the single layer and as 1.8–1.9  $\text{M}\Omega/\text{sq}$  for the multilayer. The contact resistance increases more rapidly in the single layer than in the multilayer. All the results indicate that the mobility degradation is mainly caused by the time-dependent contact resistance, and not by the sheet resistance.

#### D. Transformation of OSC films on metal electrodes

To further investigate the origin of the degradation, we conduct a structural characterization of OSC films deposited both on Cytop and PFBT-modified Au electrode surfaces. Figures 5(a)–5(f) and S12 in the Supplemental Material [33] show the surface topography map measured by AFM for single-layer and multilayer (five layers) films of Ph-BTBT-C<sub>n</sub>. We find that the images exhibit a relatively rough surface morphology in the case of a single layer on electrodes, whereas the surfaces remain flat and homogeneous for single-layer films on Cytop and multilayer films on both Cytop and electrodes. The morphology of the single-layer film on electrodes is composed of a relatively rough “base region” [observed as gray-colored areas in Figs. 5(a) and 5(e)], accompanied by “raised particles,” which are granular areas with a certain thickness (observed as white-colored areas in the same figures). The raised particles are 10–200 nm in lateral size and the step height from the base region is estimated at approximately 5 nm, as seen in Fig. 5(g). Interestingly, the step height is close to the thickness of a single molecular bilayer (5.3 nm). The lateral size and number of these raised particles increase with time, as seen in Fig. 5(h). This feature contrasts with the fairly stable surface morphology for a single layer on Cytop. It is most probable that the additional bilayer area gradually grows on top of the base region. On the other hand, we investigate whether the base region is a surface of

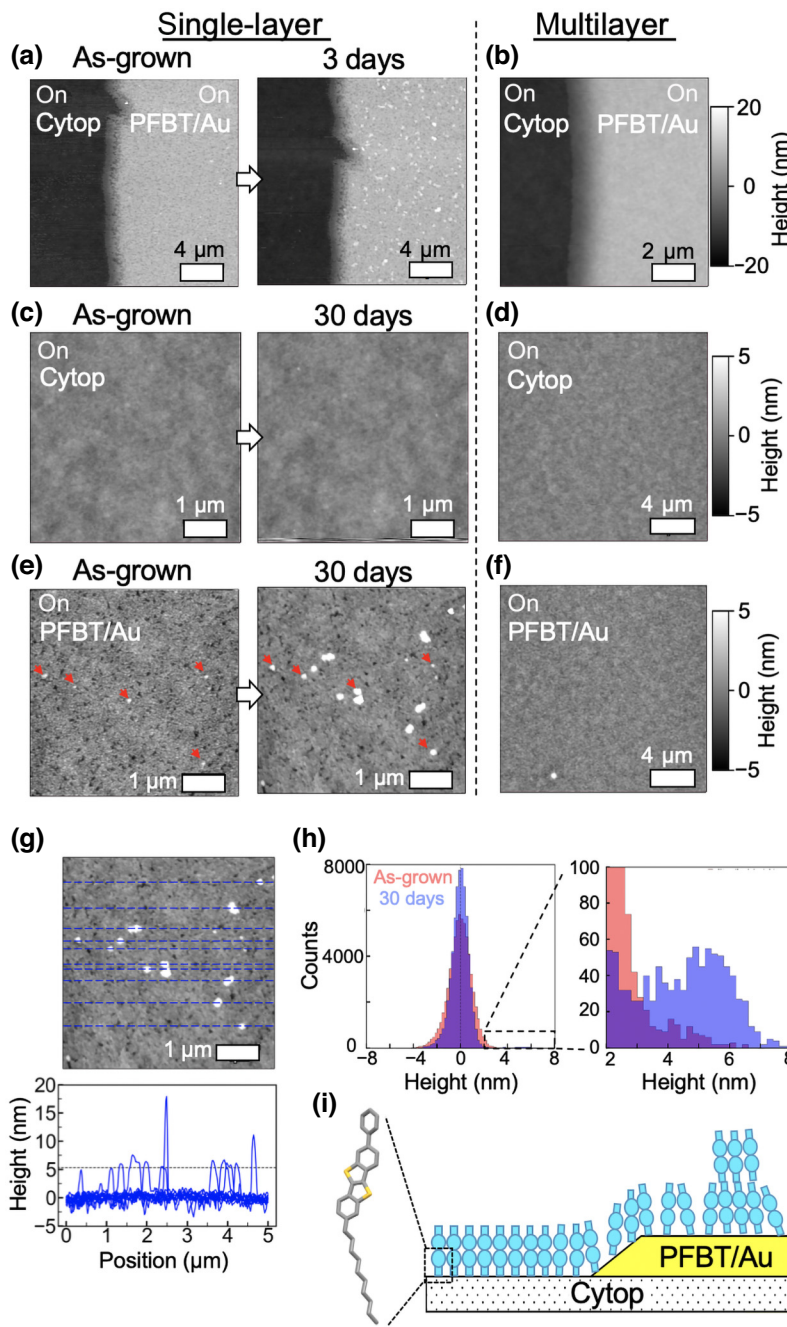


FIG. 5. Morphology of (a),(c),(e) single-layer and (b),(d),(f) multilayer (five layers) of Ph-BTBT-C<sub>n</sub> films (a),(b) around contact edge, (c),(d) on Cytop, and (e),(f) on electrodes. Images of the single-layer film show the temporal variation of a specific area. Those of the multilayer film are obtained more than one month after device fabrication. Color scale is common for each row. (g) Height profiles of the blue dashed lines on the right-hand image of (e). The black dashed line at 5.3 nm corresponds to the thickness of a single layer. (h) Statistical distribution extracted from (e). The average height of the base region corresponds to 0 nm. (i) Schematic illustration of structure of single-layer films. Single-layer film is partially defective, disordered, and stacked.

an OSC layer or a bare electrode by using crossed-Nicols microscope observations and polarized absorption measurements. We observe a clear optical anisotropy owing to Ph-BTBT-C<sub>n</sub> over the entire electrode surface with identical peak energy at about 3.3 eV [41], as seen in Figs. S13 and S14 in the Supplemental Material [33]. Therefore, it is assumed that the base region on the electrode is not a bare electrode surface but instead involves a single layer of Ph-BTBT-C<sub>n</sub> with retained crystalline anisotropy but possibly a more disordered arrangement, as shown in Fig. 5(i).

We conduct in-plane XRD measurements more than 100 h after device fabrication to investigate the

structural difference between Ph-BTBT-C<sub>n</sub> on electrodes and on Cytop. Single-domain crystal films are fabricated and extracted for the XRD measurements, as shown in Table I and Fig. 6. We first search for (020) in-plane diffractions, and then scan the  $\varphi$  angle with  $2\theta$  fixed at a specific angle corresponding to each (020) diffraction. Sharp Bragg reflections are observed for all the films, indicating that the Ph-BTBT-C<sub>n</sub> films are composed mainly of a single domain with aligned lattice spacing even for the single layer on electrodes (see also Fig. S15 in the Supplemental Material [33]). However, the peak position of the scattering vector is clearly different for the single layer

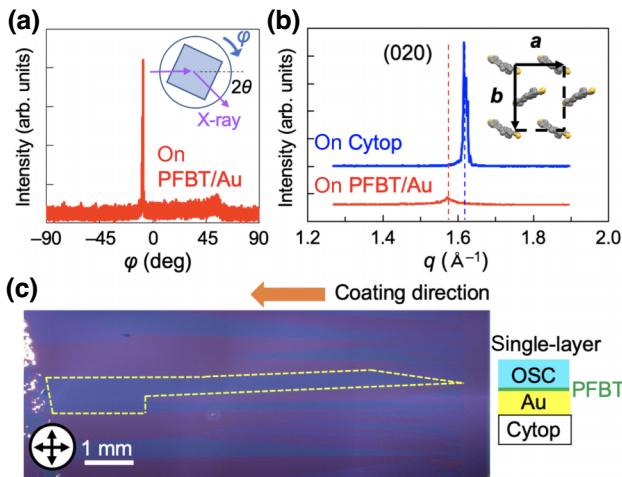


FIG. 6. In-plane x-ray diffraction (XRD) measurements of Ph-BTBT-C<sub>n</sub> films. (a) XRD profile of single layer on PFBT/Au collected by scanning the  $\varphi$  angle with  $2\theta$  fixed at  $19.88^\circ$  corresponding to the (020) diffraction. (b) XRD profile of single layer on PFBT/Au and on Cytop collected by scanning the  $2\theta$  angle with  $\varphi$  fixed at the optimal angle.  $q$  is the scattering vector. The inset is the layered-herringbone packing motif of Ph-BTBT-C<sub>10</sub>. (c) Crossed-Nicols micrograph of the single layer on PFBT/Au. The yellow dashed line shows a single-domain crystal film, as used for XRD measurements.

on electrodes compared to that on Cytop, as presented in Fig. 6(b). The  $b$ -axis length of the single layer on electrodes is estimated at  $7.98 \text{ \AA}$ , which is slightly but clearly longer than that of the bulk crystal ( $7.76 \text{ \AA}$ ) [42], whereas the value is almost the same for the single layer on Cytop ( $7.77 \text{ \AA}$ ) and for the multilayer on electrodes ( $7.70 \text{ \AA}$ ). Additionally, in  $\varphi$ -angle scanning, the peak width of the single layer on electrodes is wider than that on Cytop, indicating that the crystallinity of the single layer on electrodes is worse than that on Cytop.

Based on the results of the AFM and XRD measurements, we conclude that the single-layer films of Ph-BTBT-C<sub>n</sub> should undergo a gradual but qualitative change on electrodes, even though the single-crystalline nature seems to be preserved. We consider that the gradual change in the OSC single layer should be responsible for the contact resistance as proved by KPFM, and also for the time-dependent degradation of the device mobility.

TABLE I.  $b$ -axis length extracted from  $2\theta$  scan of XRD. The value of bulk crystal is referenced from the literature [42].

|   | Single layer<br>on Cytop | Single<br>layer on<br>PFBT/Au | Multilayer<br>on<br>PFBT/Au | Bulk<br>crystal |
|---|--------------------------|-------------------------------|-----------------------------|-----------------|
| $b$ -axis<br>length<br>( $\text{\AA}$ ) | 7.77                     | 7.98                          | 7.70                        | 7.76            |

## E. On the material and layer-number dependence of TFT characteristics

Based on the experimental results presented thus far, we discuss the origin of the material and layer-number dependence of the TFT characteristics. We first point out that the possible strain of the OSC layer due to the step of thick electrodes (25 nm) can be excluded for the observed performance deterioration in the BGBC-type organic TFTs used in this study when we consider the uniform potential drop at the contact along the channel width direction (see Fig. S10 in the Supplemental Material [33]) and the gradual and reproducible degradation of the device mobility (see Fig. S5 in the Supplemental Material [33]). We note that the height slope at the electrode edge should have a slight angle, considering the edge width of about 1  $\mu\text{m}$  against the edge height of about 25 nm.

Thus, it is reasonable to consider that the degradation of the device characteristics should be associated with the gradual and qualitative change in the ultrathin single layer on the PFBT/Au electrode surfaces caused by the relatively high surface energy or surface roughness of the electrodes. It is most probable that the material and layer-number dependence of device mobility is related to the difference in fragility or robustness of the OSC layer on the electrodes, which causes the increase in the contact resistance at the semiconductor-metal-dielectric ternary interface and eventually causes the time-dependent degradation of the device characteristics. The qualitative change in the single layer of Ph-BTBT-C<sub>n</sub> on electrodes is accompanied by a slight variation in the lattice constants while the crystalline anisotropy is maintained. Although the details of the molecular arrangement on the electrodes is not yet clear, we conjecture that the as-grown film having a quality that differs from that of the bulk crystal is the origin for the motion of OSC molecules and eventually causes the gradual film transformation, including the growth of raised particles on top of the base region. Although morphological or structural evolution has been observed in vacuum-evaporated and spin-coated OSC films [43,44], it is worth noting that a similar phenomenon occurs in single-crystalline films growing at the air-liquid interface of the meniscus [45–47]. As additional evidence of the qualitative change in the single layer, we confirm that the degradation is accelerated by heating single-layer TFTs at temperatures lower than the temperature of the liquid-crystalline transition of Ph-BTBT-C<sub>n</sub> or for the deposition of PFBT (see Fig. S16 in the Supplemental Material [33]) [30]. This result is consistent with our discussion considering that the film transformation is expected to be accelerated by the thermal motion of OSC molecules.

The degradation proceeds more slowly in some devices of the single-layer Ph-BTNT-C<sub>n</sub> TFTs than in the single-layer Ph-BTBT-C<sub>n</sub> TFTs (see Fig. S5 in the Supplemental Material [33]). This feature indicates the more robust nature of the single layer of Ph-BTNT-C<sub>n</sub> compared with

that of Ph-BTBT-C<sub>n</sub>, where the larger fused ring number is likely to be associated with the stability of the OSC layer. Additionally, significant temporal stability is obtained in the multilayer TFTs, and a similarly high stability is achieved in the encapsulated TFTs. We can consider that the bottom single bilayer, which is located closest to the electrodes and Cytop layer, works as the actual channel layer, and that the additional OSC layer or the encapsulating layer should effectively suppress the qualitative change on electrodes by restricting the motion of molecules in the bottom single bilayer. These arguments imply that the carrier conduction path is mostly restricted to the bottom single bilayer, which is consistent with the results shown in Fig. S4(a) in the Supplemental Material [33]: single-layer and multilayer TFTs exhibit similar highest mobility values ( $9 \text{ cm}^2 \text{ V}^{-1} \text{ s}^{-1}$ ). Furthermore, the effects of the atmosphere on the device characteristics present a rather peculiar behavior but can be understood in terms of the above scenario; the degradation in air becomes gradually saturated, whereas the degradation proceeds further in nitrogen gas or in vacuum, as shown in Figs. 3(c) and S7 in the Supplemental Material [33]. We consider that in the former case the absorption of some atmospheric molecules on the OSC layer or electrodes should restrict the motion of OSC molecules like an encapsulating layer, and would eventually suppress the qualitative change in the single layer.

Finally, we discuss the observed difference in the effect on the device mobility and the subthreshold characteristics; the device mobility exhibits severe time-dependent degradation, whereas the temporal variation in the value of SS and  $V_{on}$  is negligibly small. Similar features are observed in all the devices used in this study. Theoretically, the SS value is correlated with the density of carrier trap states at the semiconductor-gate dielectric interface and in the semiconductor bulk [48,49]. Therefore, the observed invariant feature of the SS value implies the highly stable nature of the semiconductor-gate dielectric interface in the channel region. Regarding the effect of the contact resistance on SS, some studies have reported that the contact resistance and SS were improved simultaneously by the insertion of the metal oxide layer [50], whereas other studies have reported that atmospheric exposure of the source and drain electrodes or adoption of different gate dielectrics causes the change in the contact resistance without affecting the SS value [21,51]. All these results clearly demonstrate that the origin of the contact resistance can be clearly separated from that of the SS values in BGBC-type TFTs when we utilize an extremely clean semiconductor-gate dielectric interface with the highly lyophobic gate dielectric layer.

#### IV. CONCLUSION

We successfully reveal the origin of the considerable channel material dependence of the device mobility

observed in extremely sharp-switching BGBC-type organic TFTs based on solution-processed, single-crystalline, and ultrathin OSC layers of Ph-BTBT-C<sub>n</sub> and Ph-BTNT-C<sub>n</sub>. We find that the device mobility crucially depends on the layer-number thickness of the OSC layers, and that the difference in the device mobility originates from the time-dependent degradation of the OSC layers on the electrodes. In particular, the single-layer Ph-BTBT-C<sub>n</sub> TFTs exhibit severe time-dependent degradation, and this feature can be ascribed to the gradual and qualitative change in the ultrathin OSC layer on the electrode surfaces as observed by AFM and XRD measurements, although the single-crystalline nature of the single layer of Ph-BTBT-C<sub>n</sub> is maintained as confirmed by crossed-Nicols microscope observation, polarized absorption spectra, and XRD measurements. The gradual and qualitative change in the OSC layer on the electrodes would be responsible for the contact resistance at the semiconductor-metal-dielectric ternary interface as observed by KPFM, which eventually causes the time-dependent degradation of the device mobility in BGBC-type TFTs. The observed qualitative transformation can be ascribed to the fragile nature of the ultrathin OSC layer on the electrodes, which depends on the OSC material. We also find that the degradation can be suppressed by using multilayer OSC films or encapsulating the channel OSC layer.

Our results demonstrate that the stability of the ternary interface is quite important in realizing the high device performance of BGBC-type organic TFTs as the most promising device configuration towards practical device applications. Understanding the stability of the ultrathin OSC layer at the ternary interface and the correlation of the component OSC molecules is crucial for attaining high performance and printed electronics applications.

#### ACKNOWLEDGMENTS

We are grateful to Dr. Mitsuhiro Ikawa for his help in the device fabrication (University of Tokyo). The synchrotron x-ray experiments were performed with the approval of the Photon Factory Program Advisory Committee (2020S2-001). This work was supported by the Japan Science and Technology Agency (JST) CREST Grant No. JPMJCR18J2 and by the Japan Society for the Promotion of Science (JSPS) KAKENHI Grants No. 21H04651, No. 20H05867, No. 20J10479, No. 21K05209, No. 21H05234, No. 22H01933, and MEXT Leading Initiative for Excellent Young Researchers Grant No. JPMXS0320220012.

- 
- [1] C. R. Kagan and P. Andry, *Thin-Film Transistors* (CRC Press, London, 2003).
  - [2] I. Kymmissis, C. D. Dimitrakopoulos, and S. Purushothaman, High-performance bottom electrode organic thin-film transistors, *IEEE Trans. Electron Devices* **48**, 1060 (2001).

- [3] J. W. Borchert, U. Zschieschang, F. Letzkus, M. Giorgio, R. T. Weitz, M. Caironi, J. N. Burghartz, S. Ludwigs, and H. Klauk, Flexible low-voltage high-frequency organic thin-film transistors, *Sci. Adv.* **6**, eaaz5156 (2020).
- [4] X. Ye, X. Zhao, S. Wang, Z. Wei, G. Lv, Y. Yang, Y. Tong, Q. Tang, and Y. Liu, Blurred electrode for low contact resistance in coplanar organic transistors, *ACS Nano* **15**, 1155 (2021).
- [5] D. J. Gundlach, L. Zhou, J. A. Nichols, T. N. Jackson, P. V. Necliudov, and M. S. Shur, An experimental study of contact effects in organic thin film transistors, *J. Appl. Phys.* **100**, 024509 (2006).
- [6] P. Cosseddu and A. Bonfiglio, A comparison between bottom contact and top contact all organic field effect transistors assembled by soft lithography, *Thin Solid Films* **515**, 7551 (2007).
- [7] J. W. Borchert, R. T. Weitz, S. Ludwigs, and H. Klauk, A critical outlook for the pursuit of lower contact resistance in organic transistors, *Adv. Mater.* **34**, 2104075 (2022).
- [8] R. Miyata, S. Inoue, K. Nakajima, and T. Hasegawa, Insulating polymer blend organic thin-film transistors based on bilayer-type alkylated benzothieno[3,2-*b*]naphtho[2,3-*b*]thiophene, *ACS Appl. Mater. Interfaces* **14**, 17719 (2022).
- [9] T. Kadoya, O. Pitayatanakul, and T. Mori, Suppression of access resistance using carbon electrodes in organic transistors based on alkyl-substituted thienoacene, *Org. Electron.* **21**, 106 (2015).
- [10] G. Kitahara, S. Inoue, T. Higashino, M. Ikawa, T. Hayashi, S. Matsuoka, S. Arai, and T. Hasegawa, Meniscus-controlled printing of single-crystal interfaces showing extremely sharp switching transistor operation, *Sci. Adv.* **6**, eabc8847 (2020).
- [11] P. Cosseddu and A. Bonfiglio, Soft lithography fabrication of all-organic bottom-contact and top-contact field effect transistors, *Appl. Phys. Lett.* **88**, 023506 (2006).
- [12] H. Iino, T. Usui, and J. I. Hanna, Liquid crystals for organic thin-film transistors, *Nat. Commun.* **6**, 6828 (2015).
- [13] J. W. Borchert, B. Peng, F. Letzkus, J. N. Burghartz, P. K. L. Chan, K. Zojer, S. Ludwigs, and H. Klauk, Small contact resistance and high-frequency operation of flexible low-voltage inverted coplanar organic transistors, *Nat. Commun.* **10**, 1119 (2019).
- [14] A. Bilgaiyan, S. Cho, M. Abiko, K. Watanabe, and M. Mizukami, Solution processed organic transistors on polymeric gate dielectric with mobility exceeding  $15 \text{ cm}^2 \text{ V}^{-1} \text{ s}^{-1}$ , *Phys. Status Solidi RRL* **14**, 2000156 (2020).
- [15] L. Bürgi, R. H. Friend, and H. Sirringhaus, Close look at charge carrier injection in polymer field-effect transistors, *J. Appl. Phys.* **94**, 6129 (2003).
- [16] C. H. Shim, F. Maruoka, and R. Hattori, Structural analysis on organic thin-film transistor with device simulation, *IEEE Trans. Electron Devices* **57**, 195 (2010).
- [17] T. J. Richards and H. Sirringhaus, Analysis of the contact resistance in staggered, top-gate organic field-effect transistors, *J. Appl. Phys.* **102**, 094510 (2007).
- [18] T. Richards and H. Sirringhaus, Bias-stress induced contact and channel degradation in staggered and coplanar organic field-effect transistors, *Appl. Phys. Lett.* **92**, 023512 (2008).
- [19] M. Koehler, I. Biaggio, and M. G. E. Da Luz, Resolving the contact voltage dilemma in organic field effect transistors, *Phys. Rev. B* **78**, 155312 (2008).
- [20] L. Merces, R. F. de Oliveira, H. L. Gomes, and C. C. Bof Bufon, The role of the electrode configuration on the electrical properties of small-molecule semiconductor thin-films, *Org. Electron.* **49**, 107 (2017).
- [21] T. Zimmerling and B. Batlogg, Improving charge injection in high-mobility rubrene crystals: From contact-limited to channel-dominated transistors, *J. Appl. Phys.* **115**, 164511 (2014).
- [22] Y. Xu, H. Sun, and Y. Y. Noh, Schottky barrier in organic transistors, *IEEE Trans. Electron Devices* **64**, 1932 (2017).
- [23] M. Gruber, E. Zojer, F. Schürrer, and K. Zojer, Impact of materials versus geometric parameters on the contact resistance in organic thin-film transistors, *Adv. Funct. Mater.* **23**, 2941 (2013).
- [24] K. Zojer, E. Zojer, A. F. Fernandez, and M. Gruber, Impact of the capacitance of the dielectric on the contact resistance of organic thin-film transistors, *Phys. Rev. Appl.* **4**, 044002 (2015).
- [25] S. W. Jo, S. Cho, and C. H. Kim, Key factors affecting contact resistance in coplanar organic thin-film transistors, *J. Phys. D: Appl. Phys.* **55**, 405101 (2022).
- [26] K. Nomoto, N. Hirai, N. Yoneya, N. Kawashima, M. Noda, M. Wada, and J. Kasahara, A high-performance short-channel bottom-contact OTFT and its application to AM-TN-LCD, *IEEE Trans. Electron Devices* **52**, 1519 (2005).
- [27] J. M. Cho and T. Mori, Low-temperature band transport and impact of contact resistance in organic field-effect transistors based on single-crystal films of Ph-BTBT-C<sub>10</sub>, *Phys. Rev. Appl.* **5**, 064017 (2016).
- [28] T. Hamai, S. Arai, H. Minemawari, S. Inoue, R. Kumai, and T. Hasegawa, Tunneling and origin of large access resistance in layered-crystal organic transistors, *Phys. Rev. Appl.* **8**, 054011 (2017).
- [29] J. Zeng, D. He, J. Qiao, Y. Li, L. Sun, W. Li, J. Xie, S. Gao, L. Pan, P. Wang, *et al.*, Ultralow contact resistance in organic transistors via orbital hybridization, *Nat. Commun.* **14**, 324 (2023).
- [30] S. Inoue, S. Shinamura, Y. Sadamitsu, S. Arai, S. Horiuchi, M. Yoneya, K. Takimiya, and T. Hasegawa, Extended and modulated thiophenes for thermally durable and solution-processable organic semiconductors, *Chem. Mater.* **30**, 5050 (2018).
- [31] T. Higashino, S. Inoue, Y. Sadamitsu, S. Arai, S. Horiuchi, and T. Hasegawa, Bilayer-type layered herringbone packing in 3-n-octyl-9-phenyl-benzothieno[3,2-*b*]naphtho[2,3-*b*]thiophene, *Chem. Lett.* **48**, 453 (2019).
- [32] T. Hamai, S. Inoue, S. Arai, and T. Hasegawa, Trap-state suppression and band-like transport in bilayer-type organic semiconductor ultrathin single crystals, *Phys. Rev. Mater.* **4**, 074601 (2020).
- [33] See Supplemental Material at <http://link.aps.org/supplemental/10.1103/PhysRevApplied.21.024005> for additional experimental results.
- [34] S. Inoue, H. Minemawari, J. Tsutsumi, M. Chikamatsu, T. Yamada, S. Horiuchi, M. Tanaka, R. Kumai, M. Yoneya, and T. Hasegawa, Effects of substituted alkyl chain length

- on solution-processable layered organic semiconductor crystals, *Chem. Mater.* **27**, 3809 (2015).
- [35] S. Arai, S. Inoue, T. Hamai, R. Kumai, and T. Hasegawa, Semiconductive single molecular bilayers realized using geometrical frustration, *Adv. Mater.* **30**, 1707256 (2018).
- [36] S. G. J. Mathijssen, M. Cölle, H. Gomes, E. C. P. Smits, B. De Boer, I. McCulloch, P. A. Bobbert, and D. M. De Leeuw, Dynamics of threshold voltage shifts in organic and amorphous silicon field-effect transistors, *Adv. Mater.* **19**, 2785 (2007).
- [37] U. Zschieschang, F. Ante, T. Yamamoto, K. Takimiya, H. Kuwabara, M. Ikeda, T. Sekitani, T. Someya, K. Kern, and H. Klauk, Flexible low-voltage organic transistors and circuits based on a high-mobility organic semiconductor with good air stability, *Adv. Mater.* **22**, 982 (2010).
- [38] L. Bürgi, H. Sirringhaus, and R. H. Friend, Noncontact potentiometry of polymer field-effect transistors, *Appl. Phys. Lett.* **80**, 2913 (2002).
- [39] Y. Yamagishi, K. Noda, K. Kobayashi, and H. Yamada, Interlayer resistance and edge-specific charging in layered molecular crystals revealed by Kelvin-probe force microscopy, *J. Phys. Chem. C* **119**, 3006 (2015).
- [40] Y. Hu, G. Li, W. Peng, and Z. Chen, Comparing the gate dependence of contact resistance and channel resistance in organic field-effect transistors for understanding the mobility overestimation issue, *IEEE Electron Device Lett.* **39**, 421 (2018).
- [41] S. Arai, K. Morita, J. Tsutsumi, S. Inoue, M. Tanaka, and T. Hasegawa, Layered-herringbone polymorphs and alkyl-chain ordering in molecular bilayer organic semiconductors, *Adv. Funct. Mater.* **30**, 1906406 (2020).
- [42] H. Minemawari, J. Tsutsumi, S. Inoue, T. Yamada, R. Kumai, and T. Hasegawa, Crystal structure of asymmetric organic semiconductor 7-decyl-2-phenyl[1]benzothieno[3,2-*b*][1]benzothiophene, *Appl. Phys. Express* **7**, 091601 (2014).
- [43] X. Chen, Z. Wang, J. Qi, Y. Hu, Y. Huang, S. Sun, Y. Sun, W. Gong, L. Luo, L. Zhang, *et al.*, Balancing the film strain of organic semiconductors for ultrastable organic transistors with a five-year lifetime, *Nat. Commun.* **13**, 1480 (2022).
- [44] T. Oka, N. Shioya, T. Shimoaka, and T. Hasegawa, Structural rearrangement of organic semiconductor molecules with an asymmetric shape in thin films, *J. Phys. Chem. C* **127**, 7560 (2023).
- [45] G. Giri, R. Li, D. M. Smilgies, E. Q. Li, Y. Diao, K. M. Lenn, M. Chiu, D. W. Lin, R. Allen, J. Reinschach, *et al.*, One-dimensional self-confinement promotes polymorph selection in large-area organic semiconductor thin films, *Nat. Commun.* **5**, 3573 (2014).
- [46] M. Yoneya, H. Minemawari, T. Yamada, and T. Hasegawa, Interface-mediated self-assembly in inkjet printing of single-crystal organic semiconductor films, *J. Phys. Chem. C* **121**, 8796 (2017).
- [47] M. R. Niazi, R. Li, M. Abdelsamie, K. Zhao, D. H. Anjum, M. M. Payne, J. Anthony, D. M. Smilgies, and A. Amassian, Contact-induced nucleation in high-performance bottom-contact organic thin film transistors manufactured by large-area compatible solution processing, *Adv. Funct. Mater.* **26**, 2371 (2016).
- [48] S. Lee, S. Jeon, and A. Nathan, Modeling sub-threshold current-voltage characteristics in thin film transistors, *J. Disp. Technol.* **9**, 883 (2013).
- [49] B. Blülle, R. Häusermann, and B. Batlogg, Approaching the trap-free limit in organic single-crystal field-effect transistors, *Phys. Rev. Appl.* **1**, 034006 (2014).
- [50] M. Kano, T. Minari, and K. Tsukagoshi, Improvement of subthreshold current transport by contact interface modification in *p*-type organic field-effect transistors, *Appl. Phys. Lett.* **94**, 143304 (2009).
- [51] G. Kitahara, M. Ikawa, S. Matsuoka, S. Arai, and T. Hasegawa, Approaching trap-minimized polymer thin-film transistors, *Adv. Funct. Mater.* **31**, 2105933 (2021).